Fabrication of Luminescent Monolayered Tungsten Dichalcogenides Quantum Dots with Giant Spin-Valley Coupling

Liangxu Lin,[†] Yaoxian Xu,[‡] Shaowei Zhang,[§,*] Ian M. Ross,[⊥] Albert C. M. Ong,[‡] and Dan A. Allwood[†,*]

[†]Department of Materials Science and Engineering, University of Sheffield, Sheffield S1 3JD, United Kingdom, [‡]Department of Infection and Immunity, University of Sheffield, Sheffield S10 2RX, United Kingdom, [§]College of Engineering, Mathematics and Physical Sciences, University of Exeter, Exeter EX4 5QF, United Kingdom, and [⊥]Department of Electronic and Electrical Engineering, University of Sheffield, S1 3JD, United Kingdom

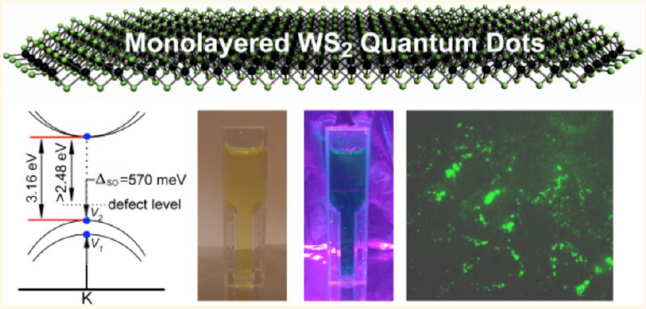

ABSTRACT A high yield (>36 wt %) method has been developed of preparing monolayered tungsten dichalcogenide (WS_2) quantum dots (QDs) with lateral size ∼8−15 nm from multilayered WS_2 flakes. The monolayered WS_2 QDs are, like monolayered WS_2 sheets, direct semiconductors despite the flake precursors being an indirect semiconductor. However, the QDs have a significantly larger direct transition energy (3.16 eV) compared to the sheets (2.1 eV) and enhanced photoluminescence (PL; quantum yield ∼4%) in the blue-green spectral region at room temperature. UV/vis measurements reveal a giant spin-valley coupling of the monolayered WS_2 QDs at around 570 meV, which is larger than that of monolayered WS_2 sheets (∼400 meV). This spin-valley coupling was further confirmed by PL as direct transitions from the conduction band minimum to split valence band energy levels, leading to multiple luminescence peaks centered at around 369 (3.36 eV) and 461 nm (2.69 eV, also contributed by a new defect level). The discovery of giant spin-valley coupling and the strong luminescence of the monolayered WS_2 QDs make them potentially of interests for the applications in semiconductor-based spintronics, conceptual valley-based electronics, quantum information technology and optoelectronic devices. However, we also demonstrate that the fabricated monolayered WS_2 QDs can be a nontoxic fluorescent label for high contrast bioimaging application.

KEYWORDS: monolayered tungsten dichalcogenides · quantum dots · luminescence · spin- valley coupling

Tungsten sulphide (WS_2) is a typical layered transition-metal dichalcogenide (LTMD) with fundamental two-dimensional (2D) building blocks (strongly bonded S−W−S layers) weakly bonded to each other by van der Waals forces.[1] This highly anisotropic bonding of WS is responsible for strongly anisotropic electrical and mechanical properties suitable for use in solid state lubricants,[2] catalytic reactions,[3] solar cells[4] and field-effect transistors (FETs).[5] New interesting properties and applications of WS_2 have been discovered on the basis of the formation of monolayered WS_2 sheets.[6] For example, WS_2 changes from an indirect to a direct band gap semiconductor with strong luminescence when converted from multilayers to monolayered sheets.[7,8] By reducing the lateral size of monolayered sheets, unique physical and chemical properties could be expected as WS_2 can be significantly affected by the edge structure and atomic defects in small nanostructures,[9] as well as quantum confinement effects emerging. Possible effects of WS_2 monolayer miniaturization include enhanced luminescent efficiency and giant spin−orbit coupling (will be confirmed in this paper) of relevance to optoelectronic and spintronic devices.

Although the exfoliation of monolayered WS_2 sheets from their bulk multilayers is well established (*e.g.,* liquid exfoliation of monolayered WS_2 sheets),[6] effective preparation of monolayered WS_2 QDs is greatly underdeveloped and their properties not well understood. In this paper, we report the effective exfoliation and disintegration of bulk WS_2

* Address correspondence to
d.allwood@sheffield.ac.uk,
s.zhang@exeter.ac.uk.

Received for review July 17, 2013
and accepted August 22, 2013.

10.1021/nn403682r

flakes to form, with high yield, monolayered WS_2 QDs of lateral size around 8–15 nm. The monolayered WS_2 QDs show a direct band gap nature, similar to monolayered sheets, which activate strong fluorescence. However, the direct gap (~3.16 eV) of the monolayered WS_2 QDs is much larger than that of monolayered WS_2 sheet (direct gap of ~2.1 eV),[8] which leads the strong photoluminescence (PL, quantum yield of ~4.0%) to be at shorter (green-blue) wavelengths than with the sheets. Unlike monolayered WS_2 sheets, the WS_2 QDs also show evidently improved giant spin-valley coupling, making them highly valuable for semiconductor-based spintronics. The spin-valley quantum states may allow future quantum entanglement of the QDs to enable quantum computation. However, in this work, due to the strong fluorescence, we also demonstrate that monolayered WS_2 QDs can be used as a nontoxic fluorescent label in confocal microscopy of biological cells.

RESULTS AND DISCUSSION

WS_2 Flake Exfoliation and Disintegration. Since WS_2 has similar layered structure to that of graphite, we exfoliate and disintegrate monolayered WS_2 QDs in the same manner we used to cut graphene QDs from graphite.[10] This includes the following steps (Scheme in Figure 1a, see Methods for more details): (1) formation of potassium intercalated WS_2 (K-WS_2, intercalation reaction) by intercalating K atoms between the covalently bonded WS2 sheets, taking advantage of the weak interlayer van der Waals force; (2) short exposure of K-WS_2 to air (deintercalation reaction); and (3) reaction between K-WS_2 and EtOH-H_2O under ultrasonication treatment. The large layer–layer distance (*d* = 6.18 Å; JCPDS: 84–1389, much larger than the *d* space of graphite) and weak van der Waals force between WS_2 layers readily allow the intercalation reaction to take place. The intercalation leads to the expansion of the layer–layer distance, which is useful for effective exfoliation and disintegration of the sheets when the K-WS_2 was exposed to air and reacted with EtOH/H_2O under ultrasonication. Although the starting (gray) and final (dark) intercalated WS_2 are not obviously different in color, scanning electron microscopy (SEM) and X-ray diffraction (XRD) observations (Figure S1) of the starting and residual WS_2 sediment strongly supported the proposed formation mechanism (shown in Figure 1a). As suggested by the SEM images and XRD patterns, the raw WS_2 materials have clear flake shape (Figure 1b,c) and are highly crystalline (Figure S1, clear diffraction pattern and strong (002) diffraction peak). By contrast, during the preparation, the WS_2 size was remarkably reduced and their edge was highly disintegrated (Figure 1d,e). XRD analysis further suggested that the

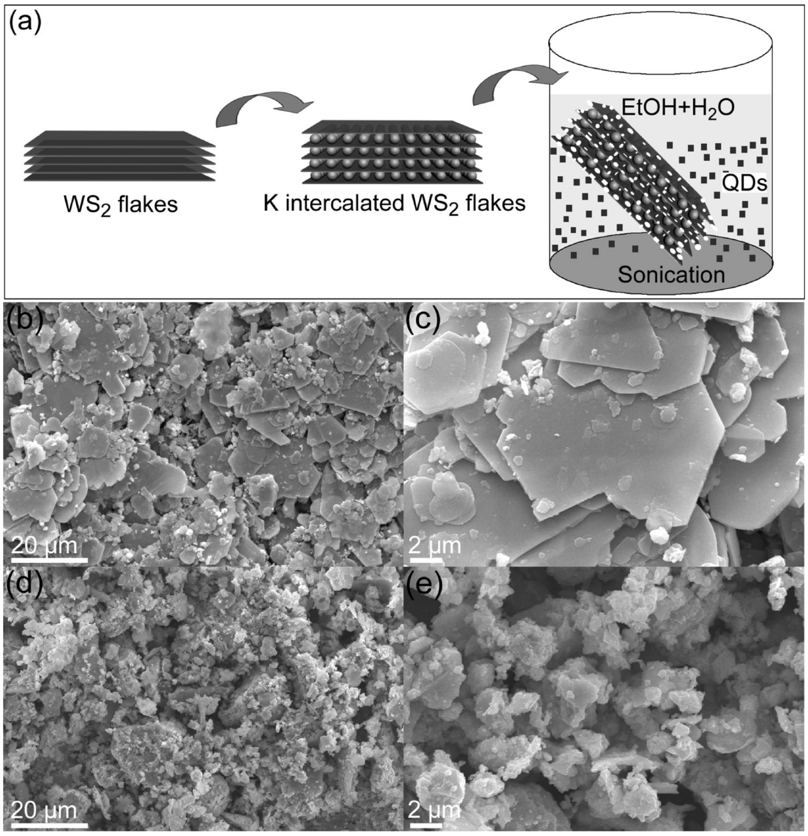

Figure 1. (a) Scheme of the preparation of monolayered WS_2 QDs. (b and c) SEM images of raw WS_2 flakes. (d and e) SEM images of the WS_2 sediment after preparation.

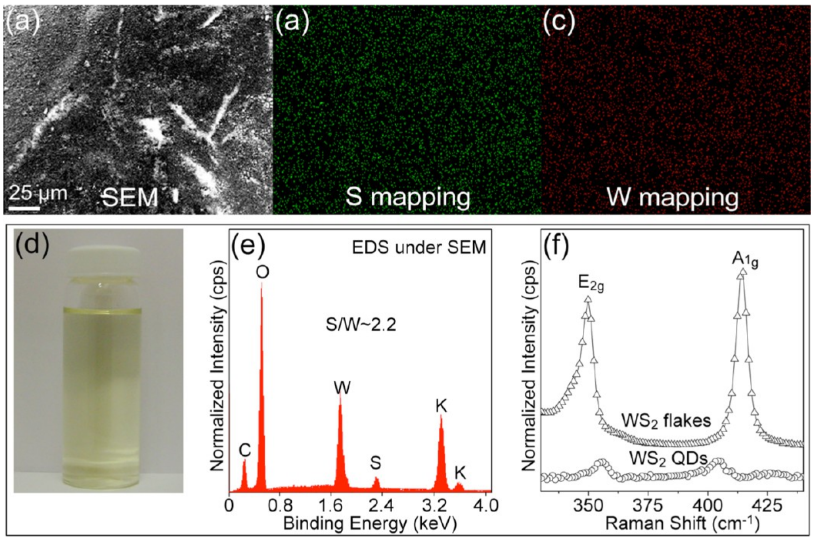

Figure 2. Characterization of the exfoliated and disintegrated WS_2 product in suspension (prior to K^+ removal): (a) SEM image and (b and c) EDS element mapping of the dried suspension; (d) photo of the suspension; (e) EDS analysis of the dried suspension under SEM observation; (d) Raman analysis of the dried suspensions.

layered structure of the WS_2 flakes was severely damaged (much weaker diffraction peak; Figure S1) due to the exfoliation and disintegration.

Characterization of Prepared WS_2 QDs. After preparation, the collected suspension (containing K^+) showed a yellow color (Figure 2d) which was stable over many months without any color or UV/vis (ultraviolet-visible) absorption changes. However, the exfoliated and disintegrated WS_2 was not stable once the K^+ in the suspension was removed using cation exchange resin (faint yellow solid S was found after a few days settling). We therefore analyzed the dried suspension (containing K^+) using XRD, EDS (energy dispersive spectroscopy), XPS (X-ray photoelectron spectroscopy) and Raman techniques, and purified WS_2 using dialysis tubing for other examinations and applications. The dried suspension (prior to K^+ removal) did not show any XRD peaks (Figure S1) from (002) diffraction of the multilayered WS_2, which suggests that the exfoliated and disintegrated products are thin structures. SEM and EDS element mappings (Figure 2a–c) confirm that the dried suspension contains W and S. Nevertheless, the measured S/W molar ratio of ~2.2 (Figure 3e, in some cases on different regions, the ratios are different but not higher than 2.5) is higher than the stoichiometric ratio of WS_2, suggesting that another S phase also existed in the dried suspension (before K removal). In the EDS spectra (Figure 2e), the C, O and K most likely arise from the chemicals involved in the preparation (K, EtOH and H_2O). Figure 2f is the Raman spectra of the dried suspension (before K removal) and WS_2 raw materials. The WS_2 raw materials show two intensive peaks around 350 and 414 cm^{-1}, corresponding to the E^1_{2g} and A_{1g} phonon modes of 2H-WS_2.[1,7] By contrast, these peaks of the dried suspension are much weaker and shift to 356 and 405 cm^{-1}, respectively, possibly due to the very thin structure of the WS_2 product and absence of layer–layer interactions.[1,7]

The chemical composition of the exfoliated and disintegrated product was further confirmed with XPS indicated that the dried suspension contained both 2H-WS_2 and K_2S phases. As shown in Figure 3, the S2p and W4f XPS show peaks at around 161.4 and 32.7 eV, respectively, consistent with those reported for 2H-WS_2 .[11−13] Deconvolution of the S2p and W4f into their components suggests that the $S2p_{3/2}$ (162.5 eV), $S2p_{1/2}$ (161.3 eV), W4f5/2 (33.4 eV), and $W4f_{7/2}$ (31.9 eV) peaks of our 2H-WS_2 are shifted to lower binding energies (shift of ~0.5 eV) compared to bulk 2H-WS_2 .[11−13] This may due to the contact between K^+ and OH^- with the WS_2 surface. In both spectra, we also found $S2p_{1/2}$ (around 15% molar ratio of all the S) from K_2S phase at around 161.2 eV[14] and W4f 3/2 of defected 2H-WS_2 bonded with surface OH^- groups at around 32.8 eV.[15] The absence of the binding peaks of tungsten oxide (W4f7/2 = 35.7 eV, W^{6+}) and tungsten hydroxide ($W4f_{7/2}$ = 36.1 eV; W^{6+})[11,12] suggests that the edges of 2H-WS_2 are S-terminated. We further analyzed the chemical composition of the dialyzed suspension (K^+ removed) using EDS under TEM observation. As shown in Figure 4a, which was taken from the agglomerated WS_2 nanoclusters shown in Figure 4b, the EDS of the dialyzed WS_2 only gives W and S signals from the nanostructures (the Cu and C are from the support grid; no O or K was found). The S/W ratio of these purified nanoclusters was around 2, which is highly consistent with the stoichiometric ratio of WS_2. It suggests that the S of the K_2S phase in the dried suspension prior to purification is more likely to be derived from WS_2 sediment rather than the exfoliated and disintegrated WS_2 product. Together with EDS analysis on different regions of the dried suspension (S/W molar ratio not higher than 2.5), by weighing the WS_2 raw material and collected sediment

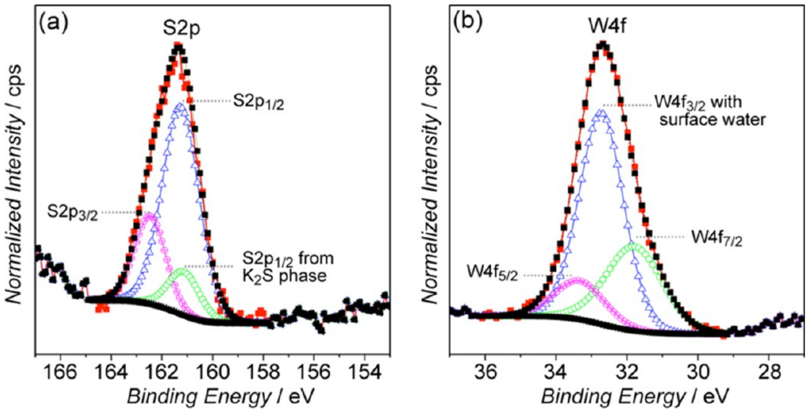

Figure 3. (a) S2p XPS of dried suspension (before K removal). (b) W4f XPS of dried suspension (before K removal).

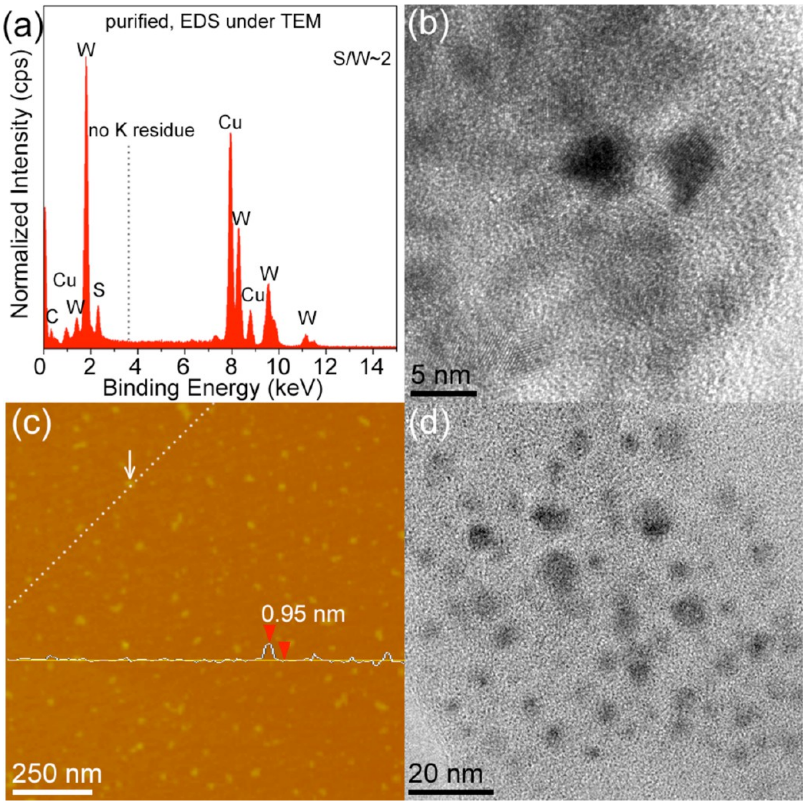

Figure 4. (a) EDS analysis taken from the region shown in (b) TEM of dialyzed WS_2 nanoclusters. (c) AFM topography image. (d) BFTEM of the dialyzed WS_2 QDs.

(mass reduced by over 45 wt %), it can be concluded that over 36 wt % WS_2 was reduced to small WS_2 dots (the morphology and size will be confirmed below).

The above results suggest that the exfoliated and disintegrated WS_2 possibly has quite small size and thin structure. To further confirm this, atomic force microscopy (AFM) and bright-field TEM (BFTEM) analysis were performed on the purified WS_2 product (using dialysis tubing). AFM (Figure 4c) and TEM (Figure 4d) observations of purified WS_2 dots both gave an average size of 8−15 nm. AFM line analysis of some dots suggests that the QDs are thin to around 0.9 nm (Figure S2). The line profile in Figure 4c gives an example, showing the thickness of 0.95 nm of the arrow indexed dot, corresponding well with that of monolayered WS_2.[7] The WS_2 dots under AFM observations should have similar thickness (reflected by their similar contrasts), which is also confirmed by a three-dimensional view of the AFM image (Figure S3). As revealed by HRTEM analysis (Figure 5), these monolayered WS_2 dots have good crystallinity. HRTEM analysis in Figure 5 also gives different information about the QDs. With these images, clear terminated edges (*e.g.,* Figure 5a, zigzag edges determined by the FFT pattern), the bond length of W−S (∼2.35 Å of 2H-WS,[16] Figure 5b), the lattice fringe of (102) with ∼2.45 Å

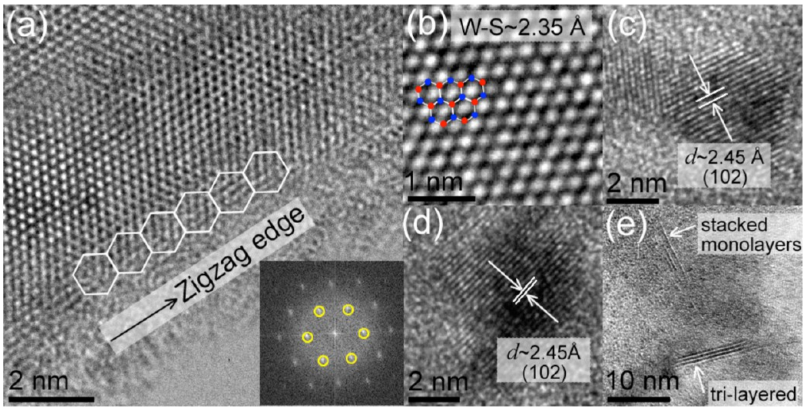

Figure 5. HRTEM images showing different information of the WS_2 QDs. Inset in image c is the FFT pattern of the crystal, showing the hexagonal structure.

(JCPDS: 84−1389) (Figure 5c,d) and hexagonal lattice structures (Figure 5a) are revealed. Some products of WS_2 flake exfoliation and disintegration were oriented side-on to the substrate, allowing direct observations of their thickness. In Figure 5e, both trilayered WS_2 with layer distances of ∼0.62 nm (lattice fringe of 002, JCPDS: 84−1389) and stacked monolayered WS_2 QDs with layer distances >1 nm are discovered.

Optical Properties of Monolayered WS_2 QDs. On the basis of the above characterizations, it is clear that high yield monolayered WS_2 QDs have been exfoliated and disintegrated from bulk WS_2 flakes. Previous studies suggested that the thickness reduction of some LTMDs (*e.g.,* WS_2, MoS) to that of monolayers resulted in a change from an indirect to a direct semiconductor.[17−19] The formation of monolayered WS_2 QDs may also lead to a similar change and interesting optical properties. Therefore, further investigation on the optical properties of the prepared monolayered WS_2 QDs was performed. Shown in Figure 6a are the UV/vis absorption spectra of the WS_2 QDs prior to purification (contains K) and purified using either ion exchange or dialysis, all exhibiting clear absorption peaks at around 277 and 393 nm. In the UV/vis spectrum of prepurified WS_2 QDs, an intense absorption peak at around 230 nm was also found, which can be attributed to the absorption from KS^-.[20] Although the K^+ in the WS_2 QDs suspension can be effectively removed using ion-exchange resin, we found that this purification normally led to the instability of WS_2 QDs as faint yellow sediment (solid S) was seen after some days of settling. This can be understood as being due to the reaction between terminating S atoms and local strong acid centers of cation exchange resin. This will leave W atoms exposed, which are easily oxidized in water solution. However, by contrast, dialyzed WS_2 QDs are stable and give similar absorption peaks, suggesting the K^+ can also be effectively removed without destroying the QD surfaces using dialysis tubing. Figure 6b shows the UV/vis spectra of dialyzed WS_2 QDs at different concentrations, in which two strong absorption peaks at around 393 nm (3.16 eV), 277 nm (4.48 eV), and one weak absorption peak at around 333 nm (3.73 eV) were found. In WS_2 nanoclusters (4−7 nm), only the strong absorption peaks at around 364 (3.41) and 295 nm (4.20 eV) were found (the weak peak between the two strong absorption peaks had disappeared).[21] The authors investigated correlating these peaks with the excitonic absorption peaks A and B of WS_2 but concluded assignment was incorrect.[21] At least the peak at the shortest wavelength cannot be attributed as excitonic absorption peak of WS_2 as no emission was found with excitation wavelength of 277 nm (4.48 eV). In monolayered WS_2 sheets, there are three absorption peaks: A, B, and optical transitions between the density of states peaks in the valence and conduction bands.[22] Therefore, the absorption peaks of 393 (3.16 eV) and 333 (3.73 eV) in our UV/vis spectra are most likely to be the excitonic absorption peaks A and B, respectively, of monolayered WS_2 QDs. The 277 nm (4.48 eV) absorption peak of the UV/vis spectra should be attributed to the optical transitions between the density of states peaks in the valence and conduction bands.[22] The A and B absorption peaks here (Figure 6b) are at noticeably shorter wavelengths than is the case with monolayered WS_2 sheets (625 and 550 nm).[22] The concentration dependent absorbance at 393 nm (Figure S4) follows the Beer−Lambert law (suggesting good water solubility of dialyzed WS_2 QDs) and yields an absorption coefficient α_{393} = 9225 $L \cdot g^{-1} \cdot m^{-1}$. This is much higher than that for A peak absorption with monolayered WS_2 sheets (2756 $L \cdot g^{-1} \cdot m^{-1}$).[6]

The strong absorption by WS_2 QDs of relatively near-UV/blue light suggests they might be capable of efficient blue or green emission. To confirm this, the room temperature PL of the dialyzed WS_2 QDs was measured under various excitation wavelengths (Figure 7a). A brief visual inspection of the QDs under UV (365 nm) illumination shows significant PL emission (Figure 7a inset). Spectral measurements of PL shows the strongest emission of the WS_2 QDs occurs at ∼461 nm (∼2.69 eV) with an excitation wavelength of 360 nm (∼3.44 eV). By using anthracene as a fluorescent standard, the luminescent quantum yield

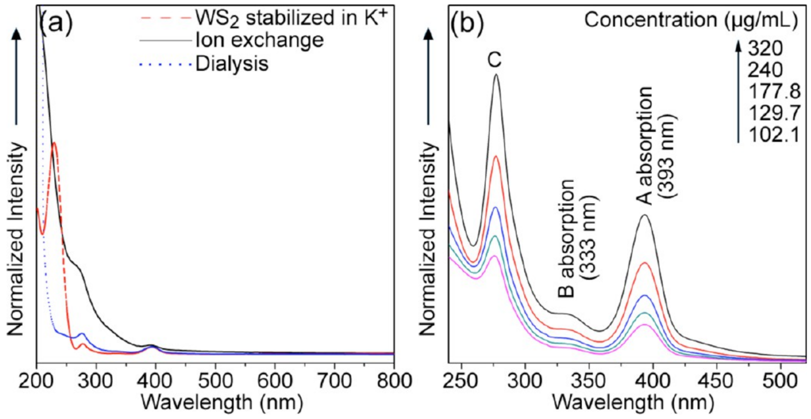

Figure 6. (a) UV/vis spectra of WS_2 QDs stabilized in K^+ and WS_2 QDs purified using different methods. For better presentation, the zero intensities of the spectra were shifted. (b) UV/vis spectra of WS_2 QDs purified using dialysis tubing.

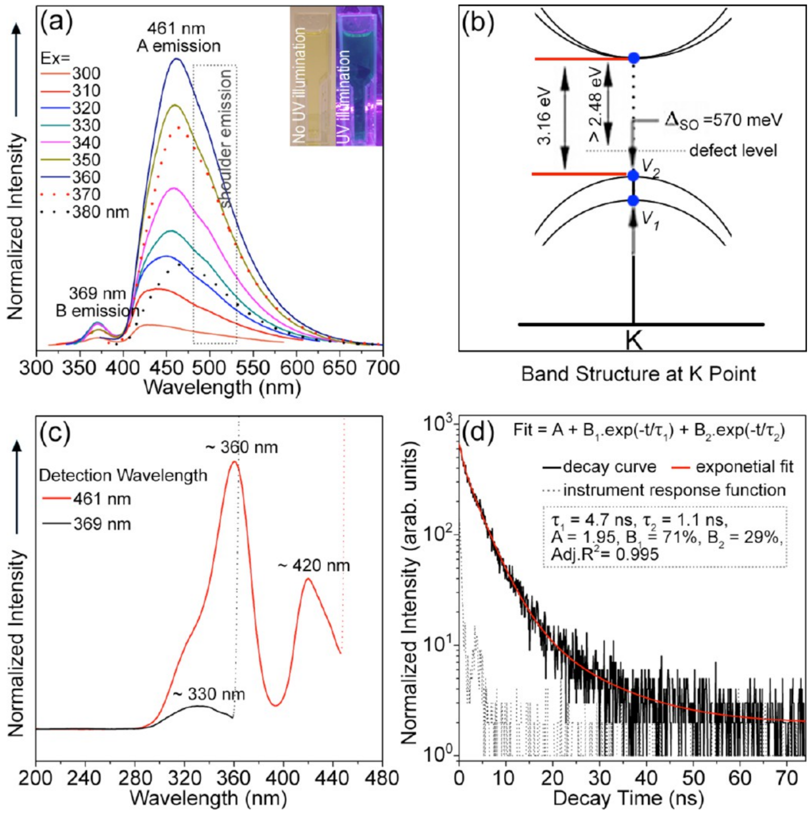

Figure 7. (a) PL spectra of dialyzed WS2 QDs with various excitation wavelengths. Inset shows photographs of the QDs with and without UV (365 nm) illumination. (b) Diagram of the band structure of purified WS2 QDs close to the K point. (c) PL excitation spectra of WS2 QDs with 369 and 461 nm detection wavelengths. (d) TRPL decay profile of WS2 QDs recorded at room temperature while monitoring the emission at 461 nm upon 360 nm excitation wavelength.

was determined as ∼4% (Table S1). This is greater than that of bulk WS_2, which exhibits only negligible luminescence due to its indirect band gap, and that of monolayered TMDC (*e.g.*, MoS_2) sheets, which remains low at about 0.4% despite their direct band gap nature.[18] Monolayered WS_2 sheets show similarly low PL quantum yields, although the reasons for this are still unclear.[22] The higher PL quantum yield observed with the monolayered WS_2 QDs may yet serve to open the way for the use of TMDCs in optical applications (*e.g.*, optoelectronic and bioimaging applications).[19]

Previous studies have found that bulk WS_2 changes to a direct gap semiconductor upon assuming monolayer thicknesses.[17,19,22,24] The increased luminescence of monolayered WS_2 QDs should depend directly on this band structure change (as described in the following, a new defect level may also contribute to the main emission at around 461 nm). However, the blue-shift of the QD PL (as well as the UV/vis spectra) compared with that of monolayered sheets (emission at 630 nm with excitonic absorption peak K at arount 625 nm)[22] may also indicate strong quantum confinement. Layered metal dichalcogenides should exhibit large quantum confinement effects.[21−24] Upon the reduction of thickness, quantum confinement effect has led to the blue shift of excitonic absorption peak A from 713 nm (1.74 eV) from bulk WS_2 to 653 nm (1.9 eV) from monolayered WS_2 sheets.[22−24] As reported for layered metal dichalcogenides, the energy shifts produced by lateral size reduction is over an order of magnitude larger than those due to thickness reduction.[25] Therefore, the large energy of excitonic absorption peak A (393 nm, compared with monolayered sheets) from our monolayered WS_2 QDs is reasonable and similar to that found from WS_2 nanoclusters (4−7 nm).[21] In the PL spectra, we also found a small emission peak at ∼369 nm (3.36 eV) and a very weak shoulder emission at ∼500 nm (2.48 eV) which might be due to a new defect level introduced in the WS_2 QDs. To understand the small emission peak at 369 nm (3.36 eV), it is necessary to consider that due to the broken inversion symmetry in monolayered WS_2, the d-orbitals of metal W atoms have strong spin−orbit coupling (a direct consequence of the giant spin-valley coupling).[24] This leads to spin splitting of the valence band, showing the largest effect at the K point of the Brillouin zone (split with an energy gap of ∼0.4 eV in monolayered WS_2 sheets).[24,26,27] This band structure is illustrated schematically in Figure 7b. The strength of this spin-valley coupling can be indicated by the energy difference (Δ_{SO}) between excitonic absorption peaks A and B in the UV/vis spectra (Figure 6b, also shown as the gap between V_1 and V_2 points in Figure 7b). On the basis of the UV/vis spectra in Figure 5b, the energy (Δ_{SO}) between V_2 (excitonic absorption peak A at 393 nm/3.16 eV) and V_1 (excitonic absorption peak B at 333 nm/3.73 eV) is 570 meV (near IR region, ∼2175 nm). This is much greater than that of monolayered WS_2 sheets (around 400 meV),[22,24] suggesting that the spin−orbit splittings of monolayered WS_2 can be manipulated by lateral size control of the QDs. Although this giant spin-valley coupling was suggested by UV/vis spectra,[6,22,24] the direct proof from PL is not always clear in monolayered WS_2 sheets.[7,22,24] In our monolayered WS_2 QDs, due to the giant spin-valley coupling, a new emission (B emission at around 369 nm, Figure 7a) from the transition between conduction band minimum and V_1 point is also discovered. Upon increasing the excitation wavelength (*Ex*) from 300 to 380 nm, the strength of the B-peak PL emission (Figure 7a) increases first before decreases again, with a maximum at *Ex* ∼ 330 nm. This result corresponds well with the UV/vis result as the maximum excitonic absorption peak B was found at around 333 nm (Figure 6b). Further PL excitation (PLE) of the monolayered WS_2 QDs, using a detection wavelength of 369 nm (B emission position in Figure 7a), only gave a broad peak around 330 nm (Figure 7c), corresponding well with UV/vis and PL results and suggesting that the B emission (∼369 nm) results from a transition between the conduction band minimum and the V_1 point (see Figure 7b). However, for the A emission (Figure 7a), a new defect level also contributed to the emission. The strength of the A-peak PL emission (Figure 7a) increases with increasing the excitation wavelength (*Ex*) from 300 to 360 nm, close to the band edge of V_2 point (393 nm). The highest emission was found at *Ex* = 360 nm instead of the maximum excitonic absorption peak A at ∼393 nm. To clarify this further, we studied the PL excitation (PLE) of the monolayered WS_2 QDs using a detection wavelength of 461 nm (A emission position in Figure 7a). We found that the PLE consisted of three peaks, including a shoulder peak at 330 nm and two strong peaks at 360 and 420 nm respectively. This suggests that the A emission (∼461 nm) of results from three contributory excitation processes: (1) excitation from the V_2 point to the conduction band minimum (360 nm excitation in PLE spectra, Figure 7c); (2) excitation from the V_1 point to the conduction band minimum (330 nm excitation in PLE spectra, Figure 7c); and (3) the last transition around 420 nm (Figure 7c) which might be the transition to the conduction band minimum from a new defect level above the valence band (Figure 7b). The contribution of the latter two transitions above results in the excitation wavelength for maximum A emission becoming shifted from 393 to 360 nm. Time resolved PL (TRPL, Figure 7d, time-correlated single photon counting technique) provided more details of these transition processes. In the TRPL curve, the lifetime of the luminescence at 461 nm can be fitted well with a biexponential function, suggesting that the decay is dominated by two of the processes discussed above (the decays of the emissions from processes 1 and 2 are the same). The observed lifetimes of the main types of luminescence are all in nanoseconds, with 71% of 4.7 ns and 29% of 1.1 ns (the decay from instrument response is 0.55 ns, see Figure S5 for more information). On the basis of the above analysis, we can conclude that the multiple PL emissions are the result of giant spin−orbit coupling of

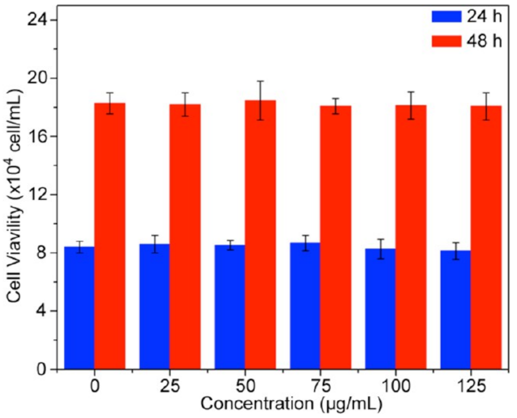

Figure 8. Cell viability assay with MDCKII cells treated with different concentrations of WS2 QDs. The bars represent cell counts and the error bars represent standard errors of the mean (SEM).

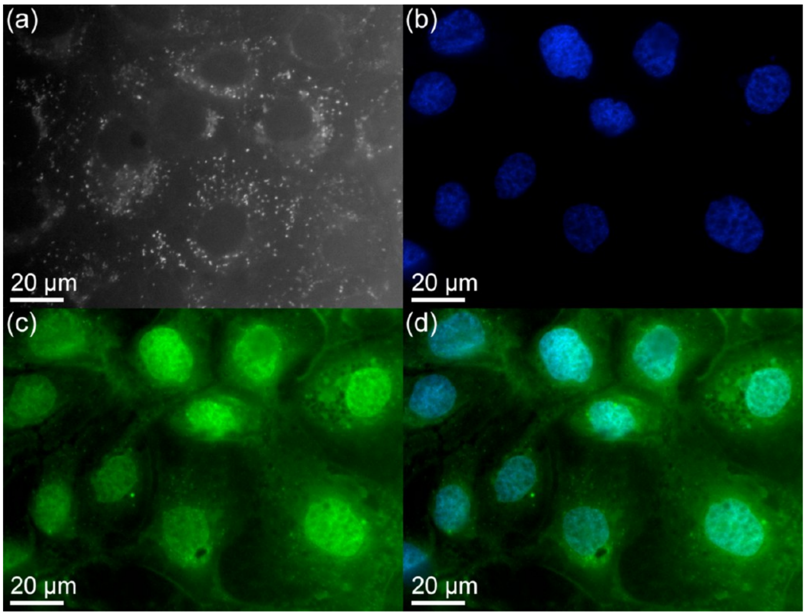

Figure 9. (a) Agglomerated WS_2 QDs surrounding each nucleus (cells are stained by WS_2 QDs only). (b) Individual nucleus stained with DAPI. (c) Cell nucleus and cytoplasm were stained with DAPI and WS_2 QDs, respectively. (d) The overlay image of panels b and c.

the monolayered WS_2 QDs, and the shift of the highest A emission is due to the additional emission contributions originate from V_1 point and a new defect level.

Bioimaging with Monolayered WS_2 QDs. The discovery of giant spin-valley coupling and modest luminescence broadens the potential applications of WS_2. For example, the nanosecond lifetime of the luminescence suggests that WS_2 QDs are potential candidate materials for optoelectronic and biological applications. However, for biological applications (*e.g.,* bioimaging, cell tracking, isolation of biomolecules, and gene technology), any possible K_2S in the WS_2 suspensions should be removed (*e.g.,* using dialysis here) to avoid cell toxicity. We evaluated the cytotoxicity of purified WS_2 QDs using the mammalian cell line MDCKII. As shown in Figure 8, low doses of WS_2 QDs (0−125 μg/mL) were nontoxic to these cells and no obvious effect on cell number was observed at these dosages (0−125 μg/mL) with prolonged exposure times (24−48 h).

To illustrate the potential in bioimaging applications, cellular imaging was performed using monolayered WS_2 QDs as fluorescent labels. The cellular imaging of the prepared WS_2 QDs was performed on MDCKII cells in fluorescein isothyocyanate (FITC) mode. Before imaging, cells were incubated with 40 μg/mL WS_2 QDs at 37 °C for 24 h. In some experiments, cell nuclei were stained with DAPI (4′,6-diamidino-2-phenylindole, Figure 9b−d) after fixation. More detailed preparation methods can be found in the Methods section. In the MDCKII cells stained with WS_2 QDs alone, the QDs were taken up by the cells but did not penetrate the cell nuclei (Figure 9a). Figure 9b,c gives the images of MDCKII nucleus stained with DAPI (emission from around 400−650 nm) and WS_2 QDs (emission from ~350−650 nm). Selection of appropriate fluorescence filters shows cell nuclei as blue (Figure 9b) or green (Figure 9c). In Figure 9c, the cytoplasm was only stained by WS_2 QDs and appears green. Although the nuclei in Figure 9c also give green emission from DAPI, the boundary between cells, nuclei and cytoplasm is clear. This is more clearly seen in the overlay image of Figure 9b and Figure 9c (Figure 9d) and suggests that WS_2 QDs can be used in high contrast bioimaging and will be well-suited for other biomedical applications.

CONCLUSION

In conclusion, we have successfully created monolayred WS_2 QDs from bulk WS_2 flakes. The majority of the QDs are monolayered with a lateral size around 8−15 nm. Like the monolayered WS_2 sheets, the monolayered WS_2 QDs also exhibit a direct semiconductor nature which is different with bulk multilayered WS_2 (indirect semiconductor) and activated strong luminescence at room temperature. The luminescence of the monolayered WS_2 QDs was found at the region of green-blue light (centered at 461 nm with multiple emission peaks) with a quantum yield of ~4% which is much improved from that of monolayered sheets. The strong luminescence and multiple emissions are considered to be the result of the direct excitonic transitions at K point and giant spin-valley coupling, respectively. As we noted, a new defect level also contributes the emission, which led to the shift of the highest main emission position. Unlike monolayered WS_2 sheets, the created monolayered WS_2 QDs have stronger spin−orbit coupling and much blue-shifted emission, suggesting the electron spin−orbit splitting and luminescence of monolayered WS$_2$ can be effectively manipulated by lateral size control, which makes them highly valuable for the applications in semiconductor based spintronics and optoelectronic devices. Further evaluations suggested that monolayered WS$_2$ QDs can be well used for biological application.

METHODS

Materials. Sigma-Aldrich WS$_2$ flakes (product no: 24639), potassium (K) chunks (product no: 244864) and Acros ethanol (product no: 181970010) were used as the main starting raw materials, and Sigma-Aldrich cation exchange resin (product no: 06423-250G) and dialysis tubing (Thermo Scientific, product no: 88242) were used to remove K$^+$ impurities from the WS QDs solutions.

Sample Preparation. About 0.6 g of K was placed into a Pyrex tube with a stop and a side vacuum connection, followed by addition of 1 g of WS$_2$ flakes. The two materials were mixed by gently shaking the Pyrex tube. The tube was heated in an oil bath to 80 °C (the temperature of the oil bath) under vacuum conditions (0.05 Torr), held for 10 min to remove any evaporable phases, and then further heated to 170−180 °C and held for >2 h. After cooling the tube to room temperature, the vacuum pump was turned off. The bottom of the Pyrex tube was placed in a room temperature water bath in an ultrasonic vibrator (Bandelin Sonorex RK-100H). Then air was introduced into the Pyrex tube rapidly by controlling the valve. Meanwhile, the ultrasonic vibrator was turned on, the stop cover of the tube was removed, and 50 mL of ethanol was poured into the tube. Once no visible K floated on the solution, 50 mL of H$_2$O was added into the tube (*Note: it is strongly recommended that the EtOH is added into the tube before the H$_2$O*). The tube was kept in the ultrasonic bath for 2 h. A yellow solution containing WS$_2$ QDs was separated from the residual solid WS$_2$ using a filter (with coarse filter paper) to remove WS$_2$ sediment. Then the collected suspension was heated in an oven to evaporate ethanol. The remaining K ions in the solution were absorbed/removed with the cation exchange resin (fill the resin into a Millipore Millicup filter unit, with ∼5 cm filling height) and dialysis tubing (Thermo Scientific, product no: 88242), respectively.

Sample Characterizations. XRD patterns were obtained using a Philips PW1830 powder diffractometer (Cu Kα, with a scanning step of 2°/min). SEM images were taken by a commercial Inspect-F SEM. UV/vis spectra were recorded by a PerkinElmer Lambda 900 Spectrometer at room temperature, and Raman spectra were recorded on a Renishaw in plus laser Raman spectrometer with λ_{exc} = 785 nm. XPS was performed on a Kratos AXIS Nova X-ray photoelectron spectrometer with an exciting source of Al K_a. The solid sample was pasted on a carbon film for the XPS analysis. The binding energy was calibrated based on C1s (284.6 eV). AFM images were taken by using a VEECO Dimension 3100 Atomic Force Microscope in a tapping mode with a scan rate of 1 Hz. A mica substrate was used for AFM analysis. TEM images were taken on a JEOL 2010F transmission electron microscope operated at 200 kV with field emission gun. Fluorescence spectra and photoluminescence excitation spectra were recorded by a Hitachi F-4500 Fluorescence Spectrophotometer at room temperature. TRPL was recorded using a time-correlated single photon counting technique with an Edinburgh Analytical Instruments F920 using picosecond pulse width laser diodes as the source of excitation.

Cytotoxicity Evaluation. The cells were cultured and maintained in DMEM (Dulbecco's Modified Eagle Medium) media (Gibco), containing 4.5g/L D-glucose, 4 mM L-glutamine, and 110 mg/mL sodium pyruvate, with 10% fetal bovine serum (FBS), 100 IU/mL penicillin and 100 μg/mL streptomycin. MDCKII cells were plated at 1.85 × 10^4 cells per well on 12-well plates, and left to adhere overnight. Different concentrations of WS$_2$ QDs (0−125 μg/mL) in culture media (50% distilled water and 50% culture media, in volume) were added to each well in triplicate. The cells were then incubated at 37 °C for 24 and 48 h, separately. At the end of each incubation, cells were gently washed with 1 mL of warm, sterile 1× PBS per well. Then 1 mL of 0.05% Trypsin-EDTA (Gibco) was added to each well which was then incubated at 37 °C for 2 h. The cells in each well were resuspended in 0.05% Trypsin-EDTA. The number of cells in each well was counted using a Hemocytometer (Hawksley, U.K.).

Cell Imaging. Two pieces of round cover glass (13 mm diameter, VWR International) were placed in a 12-well plate with 1 cover glass and 1 mL of DMEM culture medium per well. A total of 2 ×10^4 cells were plated in each well of that 12-well plate. The cells were incubated at 37 °C overnight to adhere on the cover glass. WS$_2$ QDs were added in culture medium to a final concentration of 50 μg/mL, and then the cells were incubated at 37 °C for 24 h. After incubation, the cells on two cover glasses were washed with 1 mL of 1× PBS separately. Cells were fixed using 4% paraformaldehyde at room temperature for 5 min. Then cells on cover glasses were washed with 1 mL of 1× PBS and mounted with Vectashield antifade mounting media with and without DAPI (Vector Laboratories, Inc., Burlingame, CA), respectively. Cellular images were taken using the Olympus IX71 inverted research microscope equipped with the Olympus DP70 Color/Black and White camera (Olympus, America). An Olympus U-RFL-T power supply unit with a mercury lamp was used as the fluorescence light source.

Conflict of Interest: The authors declare no competing financial interest.

Supporting Information Available: Further characterization of WS$_2$ QDs. This material is available free of charge *via* the Internet at http://pubs.acs.org.

Acknowledgment. This work was supported by the University of Sheffield. We thank Prof. C. A Hunter, Miss H. Sun, Dr. A. Barlow and Dr. En Ma for the assistance with the fluorescence, XPS and TRPL analysis

REFERENCES AND NOTES

1. Molina-Sánchez, A.; Wirtz, L. Phonons in Single-Layer and Few-Layer MoS$_2$ and WS$_2$. *Phys Rev. B* **2011**, *84*, 155413.
2. Rapoport, L.; Fleischer, N.; Tenne, R. Fullerene-like WS$_2$ Nanoparticles: Superior Lubricants for Harsh Conditions. *Adv. Mater.* **2003**, *15*, 651–655.
3. Merki, D.; Hu, X. Recent Developments of Molybdenum and Tungsten Sulfides as Hydrogen Evolution Catalysts. *Energy Environ. Sci.* **2011**, *4*, 3878–3888.
4. Wu, M.; Wang, Y.; Lin, X.; Yu, N.; Wang, L.; Wang, L.; Hagfeldt, A.; Ma, T. Economical and Effective Sulfide Catalysts for Dye-Sensitized Solar Cells as Counter Electrodes. *Phys. Chem. Chem. Phys.* **2011**, *13*, 19298–19301.
5. Hwang, W. S.; Remskar, M.; Yan, R.; Protasenko, V.; Tahy, K.; S. Chae, D.; Zhao, P.; Konar, A.; Xing, H.; Seabaugh, A.; *et al.* Transistors with Chemically Synthesized Layered Semiconductor WS$_2$ Exhibiting 10^5 Room Temperature Modulation and Ambipolar Behavior. *Appl. Phys. Lett.* **2012**, *101*, 013107.
6. Coleman, J. N.; Lotya, M.; O'Neill, A.; Bergin, S. D.; King, P. J.; Khan, U.; Young, K.; Gaucher, A.; De, S.; Smith, R. J.; *et al.* Two-Dimensional Nanosheets Produced by Liquid Exfoliation of Layered Materials. *Science* **2011**, *331*, 568–571.
7. Gutiérrez, H. R.; Perea-López, N.; Elías, A. L.; Berkdemir, A.; Wang, B.; Lv, R.; López- Urías, F.; Crespi, V. H.; Terrones, H.; Terrones, M. Extraordinary Room-Temperature Photoluminescence in Triangular WS$_2$ Monolayers. *Nano Lett.* **2013**, *13*, 3447–3454.
8. Jiang, H. Electronic Band Structures of Molybdenum and Tungsten Dichalcogenides by the GW Approach. *J. Phys. Chem. C* **2012**, *116*, 7664–7671.
9. Liu, Z.; Suenaga, K.; Wang, Z.; Shi, Z.; Okunishi, E.; Iijima, S. Identification of Active Atomic Defects in A Monolayered Tungsten Disulphide Nanoribbon. *Nat. Commun.* **2011**, *2*, 213.

10. Lin, L.; Zhang, S. Creating High Yield Water Soluble Luminescent Graphene Quantum Dots *via* Exfoliating and Disintegrating Carbon Nanotubes and Graphite Flakes. *Chem. Commun.* **2012**, *48*, 10177–10179.
11. Martin-Litas, I.; Vinatier, P.; Levasseur, A.; Dupin, J. C.; Gonbeau, D.; Weill, F. Characterisation of r.f. Sputtered Tungsten Disulfide and Oxysulfide Thin Films. *Thin Solid Films* **2002**, *4156*, 1–9.
12. Martinez, H.; Benayad, A.; Gonbeau, D.; Vinatier, P.; Pecquenard, B.; Levasseur, A. Influence of the Cation Nature of High Sulfur Content Oxysulfide Thin Films MO_yS_z (M = W, Ti) Studied by XPS. *Appl. Surf. Sci.* **2004**, *236*, 377–386.
13. Dartigeas, K.; Gonbeau, D.; Pfister-Guillouzo, G. Core and Valence Spectra of TaS_2 and WS_2. Experimental and Theoretical Studies. *J. Chem. Soc., Faraday Trans.* **1996**, *92*, 4561–4566.
14. Yu, X.; Liu, F.; Wang, Z.; Chen, Y. Auger Parameters for Sulfur-Containing Compounds Using A Mixed Aluminum-Silver Excitation Source. *J. Electron Spectrosc. Relat. Phenom.* **1990**, *50*, 159–166.
15. Shpak, A. P.; Korduban, A. M.; Kulikov, L. M; Krvshchuk, T. V.; Konig, N. B.; Kandvba, V. O. XPS Studies of The Surface of Nanocrystalline Tungsten Disulfide. *J. Electron Spectrosc. Relat. Phenom.* **2010**, *181*, 234–238.
16. Gordon, R. A.; Yang, D.; Crozier, E. D.; Jiang, D. T.; Frindt, R. F. Structures of Exfoliated Single Layers of WS_2, MoS_2, and $MoSe_2$ in Aqueous Suspension. *Phys. Rev. B* **2002**, *65*, 125407.
17. Ramasubramaniam, A. Large Excitonic Effects in Monolayers of Molybdenum and Tungsten Dichalcogenides. *Phys. Rev. B* **2012**, *86*, 115409.
18. Mak, K. F.; Lee, C.; Hone, J.; Shan, J.; Heinz, T. F. Atomically Thin MoS_2: A New Direct-Gap Semiconductor. *Phys. Rev. Lett.* **2010**, *105*, 136805.
19. Wang, Q. H.; Kalantar-Zadeh, K.; Kis, A.; Coleman, J. N.; Strano, M. S. Electronics and Optoelectronics of Two-Dimensional Transition Metal Dichalcogenides. *Nat. Nanotechnol.* **2012**, *7*, 699–712.
20. Karge, H. G.; Raskó, J. Hydrogen Sulfide Adsorption on Faujasite-Type Zeolites with Systematically Varied Si-Al Ratios. *J. Colloid Interface Sci.* **1978**, *64*, 522–532.
21. Huang, J. M.; Laitinen, R. A.; Kelley, D. F. Spectroscopy and Tapping Dynamics in WS_2 Nanoclusters. *Phys. Rev. B* **2000**, *62*, 10995–11005.
22. Zhao, W.; Ghorannevis, Z.; Chu, L.; Toh, M.; Kloc, C.; Tan, P.-H.; Eda, G. Evolution of Electronic Structure in Atomically Thin Sheets of WS_2 and WSe_2. *ACS Nano* **2013**, *7*, 791–797.
23. Kam, K. K.; Parkinson, B. A. Detailed Photocurrent Spectroscopy of the Semiconducting Group VIB Transition Metal Dichalcogenides. *J. Phys. Chem.* **1982**, *86*, 463–467.
24. Zeng, H.; Liu, G.-B.; Dai, J.; Yan, Y.; Zhu, B.; He, R.; Xie, L.; Xu, S.; Chen, X.; Yao, W.; Cui, X. Optical Signature of Symmetry Variations and Spin-Valley Coupling in Atomically Thin Tungsten Dichalcogenides. *Sci. Rep.* **2013**, *3*, 1608.
25. Wilcoxon, J. P.; Newcomer, P. P.; Samara, G. A. Synthesis and Optical Properties of MoS_2 and Isomorphous Nanoclusters in the Quantum Confinement Regime. *J. Appl. Phys.* **1997**, *81*, 7934–7944.
26. Xiao, D.; Liu, G.-B.; Feng, W.; Xu, X.; Yao, W. Coupled Spin and Valley Physics in Monolayers of MoS_2 and Other Group-VI Dichalcogenides. *Phy. Rev. Lett.* **2012**, *108*, 196802.
27. Zhu, Z. Y.; Cheng, Y. C.; Schwingenschlögl, U. Giant Spin-Orbit-Induced Spin Splitting in Two-Dimensional Transition-Metal. *Phys. Rev. B* **2011**, *84*, 153402.